Supporting information for

The influence of fluorine spin-diffusion on ^{13}C solid-state NMR line shapes of CF$_3$ groups

Ettore Bartalucci[a,b], Calogero Quaranta[c], Fabio Manzoni[d], Igor d'Anciães Almeida Silva[a,e], Mirijam Zobel[d,f], Carsten Bolm[c], Matthias Ernst[g,*], and Thomas Wiegand[a,b,*]

[a] Max Planck Institute for Chemical Energy Conversion, Stiftstr. 34–36, 45470 Mülheim/Ruhr, Germany

[b] Institute of Technical and Macromolecular Chemistry, RWTH Aachen University, Worringerweg 2, 52074 Aachen, Germany

[c] Institute of Organic Chemistry, RWTH Aachen University, Landoltweg 1, 52074 Aachen, Germany

[d] Institute of Crystallography, RWTH Aachen University, Jagerstrasse 17–19, 52066 Aachen, Germany

[e] present address: NMR facility, University of Missouri, 601 S. College Avenue, MO 65211, United States

[f] JCNS-3: Neutron Analytics for Energy Research, Forschungszentrum Jülich GmbH, Wilhelm-Johnen-Straße, 52428 Jülich, Germany

[g] Physical Chemistry, ETH Zürich, Vladimir-Prelog-Weg 2, 8093 Zürich, Switzerland

*: Corresponding authors. maer@ethz.ch and thomas.wiegand@cec.mpg.de

Experimental Section

Sample preparation

Both, racemic and enantiopure ((*R*) and (*S*)) crystalline compounds of TFLA have been purchased from BLDpharm. The milled (*R*)- and (*S*)-TFLA samples were prepared separately, each using a 1.5 mL stainless-steel milling jar from Retsch, which was loaded with the sample (60 mg and 70 mg, respectively) and one 7 mm stainless-steel ball[1]. The sample was milled for 20 min at 25 Hz in a MM400 vibrational ball mill from the company Retsch. The sample was then scraped off the milling jar and analysed with solid-state NMR.

The supported ionic liquid phase (SILP) sample containing bistriflimide NTf_2^- has been prepared according reference [2].

The 4-(trifluoromethyl)benzene-1-carboximidamide hydrochloride hydrate sample has been purchased from Maybridge.

Solid-state NMR

A comprehensive overview of the experimental parameters used for the acquisition of the solid-state NMR spectra in this study is reported in Table S2.

^{13}C-detected ^1H-^{13}C and ^{19}F-^{13}C cross-polarization (CP) and dipolar-dephasing (DD) experiments were acquired at 11.7 and 16.4 T static external magnetic-field strengths in Bruker 3.2 mm (standard double-resonance, standard triple-resonance, E-free triple-resonance) and 1.3 mm (standard double-resonance) probes.

Except where specified, ^{13}C-detected ^1H-^{13}C CP and DD spectra were recorded under high-power SPINAL-64 ^1H decoupling[3] during data acquisition.

In the case of MAS-dependent ^1H-^{13}C CP experiments for TFLA the MAS frequency was set to 14.0 kHz, 17.5 kHz and 22.0 kHz in a 3.2 mm probe and 30.0 kHz, 40.0 kHz, 50.0 kHz and 60.0 kHz in a 1.3 mm probe (see Table S2).

^{13}C-detected ^1H-^{13}C DD experiments were recorded at 20.0 kHz MAS frequency at 11.7 T static magnetic-field strength using dephasing delays of 100 μs, 200 μs and 300 μs for testing the suppression efficiency of non-quaternary carbon resonances. Taking the optimal one, only the spectrum recorded with dephasing delay of 300 μs is shown in Figure S6.

The series of ^{19}F-^{13}C CP experiments with off-resonance ^{19}F decoupling was recorded at 15.0 kHz MAS frequency and 11.7 T static magnetic-field strength, while varying the angle θ of the effective ^{19}F-field with respect to B_0 during continuous-wave (CW) decoupling between

20° to 90° (see Table S2). The other ^{19}F-^{13}C CP experiments were acquired either without ^{19}F decoupling or under high-power SPINAL-64 ^{19}F decoupling during data acquisition.

^{19}F-^{13}C CP experiments under 45 kHz SW$_f$-TPPM ^{1}H decoupling[4] were recorded in a Bruker 4.0 mm probe at 12.5 kHz MAS and 11.7 T static magnetic-field strength.

Static ^{19}F Hahn echo spectra were recorded at 11.7 T static magnetic-field strength with a standard Bruker 3.2 mm triple-resonance probe. Under the same conditions, static T_2 echo-decay curves for both racemic and enantiopure TFLA samples were recorded. The decay profile was determined by manual two-components fitting of each 1D ^{19}F spectrum recorded as a function of echo delay, using as fitting parameters for (*S*)-TFLA a pure Lorenzian line for the sharp peak and a 50% Lorenzian – 50% Gaussian line for the broad component with fixed position and width, while for *rac*-TFLA a pure Lorenzian line for the sharp peak and a 70% Lorenzian – 30% Gaussian line for the broad component, with variable amplitude, position and width. The fitting procedure was carried out using DMFIT.[5] Subsequent estimation of T_2 values was performed using a standard exponential decay fit in MATLAB (MATLAB, The MathWorks Inc.) with the *lsqcurvefit* module. ^{19}F Hahn echo spectra under MAS were recorded at 17.0 kHz and under the same conditions as the static case.

^{13}C T_1 values for *rac*- and (*S*)-TFLA were determined using the relaxation module of Topspin 4.1.4, from experimental data measured with a standard ^{1}H-^{13}C CP T_1 experiment, recorded in a Bruker 3.2 mm triple-resonance probe at 17.5 kHz MAS and 16.4 T static magnetic-field strength.^{19}F T_1-values for both *rac*- and (*S*)-TFLA were determined by a standard saturation-recovery experiment using ssNake,[6] recorded with a 3.2 mm triple-resonance probe at 20 kHz MAS and 11.7 T magnetic field strength.

In all cases, ^{13}C spectra were referenced to an adamantane standard based on the tetramethyl silane (TMS) scale, for which the methylene resonance of adamantane is set to 38.56 ppm,[7] while ^{19}F experiments were referenced to sodium tetrafluoroborate (NaBF$_4$, ^{19}F resonance set to -159.2 ppm[8]) standard based on the trichlorofluoromethane scale. The standard was recorded in the same probe directly before the measurements. Except for specified cases, for the static spectra and for the ones in a 4.0 mm Bruker probe, all other measurements were carried out with temperature control. For the target VTU temperatures settings used during acquisition and further experimental parameters we refer to Table S2.

All spectra were processed with the software Topspin (versions 3.6.5, 4.1.3 and 4.3.0, 4.4.0 Bruker Biospin).

General information for data analysis

For the first implementation of a functioning python script for the calculation of the homonuclear ^{1}H-^{1}H and ^{19}F-^{19}F van-Vleck second moments as well as for debugging purposes during writing the MATLAB script (MATLAB, The MathWorks Inc.) to compute χ^2 statistics, ChatGPT (GPT-3.5 and GPT-4o, OpenAI[9]) has been used as support.

Calculation of the square root of the sum of squared dipolar couplings

The square root of the sum of squared dipolar couplings for nucleus i, d_i^{RSS}, as defined in equation (S1)[10, 11] has been calculated based on either the time averaged distances of the fluorine atoms under fast rotation. This corresponds to calculating the dipolar couplings based on the distances between the centers of gravity of the fluorine atoms in each CF_3 group. Alternatively, also the averaged dipolar couplings have been calculated by assuming uncorrelated motion of the methyl groups on a circle and averaging over the dipolar couplings.

$$d_i^{RSS} = \frac{\mu_0}{8\pi^2}\gamma_F^2 \sqrt{\sum_j \left(\frac{1}{r_{i,j}^3}\right)^2} \qquad \text{(S1)}$$

Simulation of 1D ^{13}C spectra for the CF_3 group

The script for simulating the changes in self-decoupling for ^{13}C spectra as a function of k_{ex} has been written in MATLAB (MATLAB, The MathWorks Inc.) based on an initial implementation of the Bloch-McConnel equations in Mathematica (Wolfram Research, Inc.) providing as input values the experimental strength of the ^{19}F-^{13}C J-coupling (280 Hz), values of k_{ex} between 1 s^{-1} and 7500 s^{-1} and a fixed T_2-value of 0.03 s (FWHM = 10 Hz).

Non-linear least-square peak fitting

The script performing a 1D non-linear least-square fit of the experimental and simulated ^{13}C spectra has been performed using the built-in function *lsqcurvefit* in MATLAB (MATLAB, The MathWorks Inc.) with variable k_{ex} and T_2 parameters.

The confidence intervals for the k_{ex} values, which are reported in Figure 3, have been calculated as standard errors (S.E.) from the covariance matrix of the fits as follows:

$S.E. = \sqrt[2]{diag(Cov)}$

where the covariance matrix **Cov** is given by:

$Cov = (J' * J)^{-1} * \sigma^2$

In this equation J is the Jacobian obtained from the non-linear least-square fit and σ^2 is the estimate of the residual variance, calculated from the residuals R, the number of observations N and the number of estimated coefficients p, as follows:

$$\sigma^2 = \frac{R}{N - p}$$

The resulting k_{ex} and T_2 values are listed in the table below.

MAS / kHz	rac-TFLA k_{ex} / s^{-1}	rac-TFLA T_2 / s (FWHM / Hz)	(S)-TFLA k_{ex} / s^{-1}	(S)-TFLA T_2 / s (FWHM / Hz)
60.0	0.0 ± 0.3	0.0120 (26)	17.3 ± 0.9	0.0115 (28)
50.0	0.0 ± 0.5	0.0159 (20)	29.5 ± 1.0	0.0131 (24)
40.0	34.5 ± 0.8	0.0178 (18)	88.9 ± 1.7	0.0194 (16)
30.0	48.8 ± 0.9	0.0150 (21)	155.8 ± 1.4	0.0146 (22)
22.0	72.2 ± 0.8	0.0136 (23)	302.8 ± 2.1	0.0128 (25)
17.5	102.5 ± 0.9	0.0105 (30)	537.6 ± 1.6	0.0104 (31)
14.0	188.6 ± 1.2	0.0105 (30)	675.1 ± 2.7	0.0106 (30)

Minimum-χ^2 estimation

The script for calculating the minimum-χ^2 value between experimental and simulated ^{13}C spectra as a function of k_{ex} and T_2 has been written in MATLAB (MATLAB, The MathWorks Inc.). To this end, the χ^2 values were calculated by simulating ^{13}C spectra according to Bloch-McConnel equations (*vide infra*) over a range of 50 values of k_{ex} adjusted around the respective k_{ex} minima for each spectrum and 50 values of T_2 between 0 s and 0.1 s, and computing the minimum-χ^2 with respect to the experimental spectra according to the following equation:

$$\chi^2 = \sum_{i=1}^{k} (O_i - E_i)^2 \#(S2)$$

Where the O_i represent the simulated spectra and E_i represent the experimental spectra.

Numerical simulations of off-resonance ^{19}F decoupled spectra as a function of θ

Spectra under off-resonance irradiation were simulated using the spin-simulation environment GAMMA,[12] using the geometry of a fast motionally averaged CF_3 group with all tensors being

axially symmetric and scaled by the rotation ($\delta_{CF}/2\pi$ = 7.87 kHz, $\delta_{FF}/2\pi$ = 10.7 kHz, $\delta_F/2\pi$ = 26.352 kHz, J_{CF} = −280 Hz, J_{FF} = 100 Hz). The MAS rotation (15.0 kHz) was implemented using time slicing with 100 points on the rotor period. Spin diffusion between the ^{19}F was simulated using a random-field relaxation super operator.[13] Using an initial state of $\sigma_0 = S_x$ and a detection operator S^+, the density operator was evolved under the propagator for a full rotor period. The FID was Fourier transformed using additional line broadening by exponential apodization.

Correlating dipolar coupling network to changes in SD rate constants

From a comparison of the crystal structures, interestingly face-to-face dimers are observed for (*S*)-TFLA, whereas for *rac*-TFLA a displacement of the groups relative to each other is observed (Figure 2b). The intramolecular carbon-carbon distance between two facing CF_3 groups is ~ 4.13 Å for the racemic dimers while is ~ 4.16 Å for the enantiopure dimers (see Table S1).

Table S1: Data collections for correlating dipolar coupling network to changes in SD rate constants for *rac*-TFLA and (*S*)-TFLA. The center of mass ("center") assumes that the F are located in the center of the circle spanned by the three fluorine atoms of the CF_3 group, while the "circle" takes an explicit averaging over all possible combinations on the circle into account and assumes an "uncorrelated" rotations of the involved CF_3 groups.

Sample	Static [19]F T_2 / ms	d_i^{RSS} center / kHz	d_i^{RSS} circle / kHz	$^{13}C_{CF3}$-$^{13}C_{CF3}$ / Å	$^{13}C_{CF3}$ T_1 / s	[19]F T_1 / s
rac-TFLA	1.98	11.4	10.6	4.13	2.3	1.4
(*S*)-TFLA	1.96	11.6	9.7	4.16	1.0	1.0

How commonly are CF₃ group resonances affected by ¹⁹F SD? Two further examples.

To probe whether the line-broadening mechanism observed for (*S*)-TFLA at slow MAS frequencies can be generalized to other molecules containing CF_3 groups, we investigated two additional samples, a supported-ionic liquid phase (SILP) containing bistriflimide as an anion (**1**), and the organic molecule 4-(trifluoromethyl)benzene-1-carboximidamide hydrochloride hydrate (**2**) (for the chemical structures see Figure S6a). As can be observed in Figure S6b, ^{13}C-detected [19]F-^{13}C CP spectra (in the absence of ^{19}F high-power decoupling) for the SILP sample

clearly shows the expected sharp quartet, indicating a slow-exchange regime ($k_{ex} \ll 2\pi J_{CF}$) in this case.

For compound (**2**), spectral overlap of the CF_3 group and aromatic carbons complicate the analysis of the ^1H-^{13}C CP spectrum and a ^{13}C dipolar-dephasing (DD) CP-MAS spectrum has been recorded to reduce overlap (Figure 6c). Although the aromatic carbon atoms are not fully suppressed in the latter spectrum, a resolved quartet line shape for the CF_3 group is already clearly identified. To selectively excite the CF_3 group carbon resonance, we next turned to ^{13}C-detected ^{19}F-^{13}C CP spectra applying ^{19}F (Figure S6d (I)) and ^1H heteronuclear decoupling (Figure S6d (II)) as well as recording the spectrum in the absence of heteronuclear decoupling (Figure S6d (III)). A short CP contact time has been used to only transfer ^{19}F polarization to the directly-bound carbon atom of the CF_3 group. For the ^{19}F-^{13}C CP spectrum in Figure S6d we can indeed observe the ^{13}C resonance corresponding to the CF_3 group, that is still significantly broadened, but clearly reveals the quartet multiplet structure. Line broadening might be caused by a sizeable inhomogeneous contribution to the NMR linewidth, for instance caused by anisotropic bulk magnetic susceptibility effects[10, 14, 15] as already reported for fluorinated molecules.[16] Recording the spectra with ^1H decoupling only slightly improves the resolution. Interestingly, the relative peak intensities for the partially resolved quartet differ from the expected 1:3:3:1 ratio. We currently further explore this effect in our laboratories and attribute it to the faster CP-polarization build-up for the quartet associated with a group spin $\hat{F} = \dfrac{3}{2}$, compared to the central two doublets associated with $\hat{F} = \dfrac{1}{2}$.[17]

Powder X-Ray Diffraction (PXRD)

The crystal structure of (*S*)-TFLA was studied by performing Powder X-ray Diffraction (PXRD) on a Bruker AXS D8 Advance diffractometer equipped with a Cu-tube and a Ni-filter at a tube voltage of 40kV and a current of 40 mA. The measurement was performed with a LynxEye detector at room temperature in the 2θ range of 10-60° with a step size of 0.0105°.

The crystal structure was refined by using the Rietveld method[18] performed with the Topas academic software (Version 7.21; Cheary and Coelho[19]).

Since the indexing of the pattern suggested a structure belonging to the space group C_2, the deposited structure of the (*S*)-TFLA (CSD number: 666327) was used as a starting point for the refinement.[20]

During the refinement, a six-coefficient polynomial was used to describe the background, while the lattice parameters a, b, c and β were free to vary. Due to the low symmetry of the system (space group C_2), the positions of the atoms were fixed.

The intensity of the peaks at 17.75°, 18.15°, 19.65° and 30.65°, suggested a strong preferential orientation on at least 4 directions: (100), (001), (10-1), (101). In order to model this behaviour, the March-Dollase approach was used.[21]

The PXRD pattern is shown in Figure S5, while the results are summarised in Table S3.

Supplementary figures
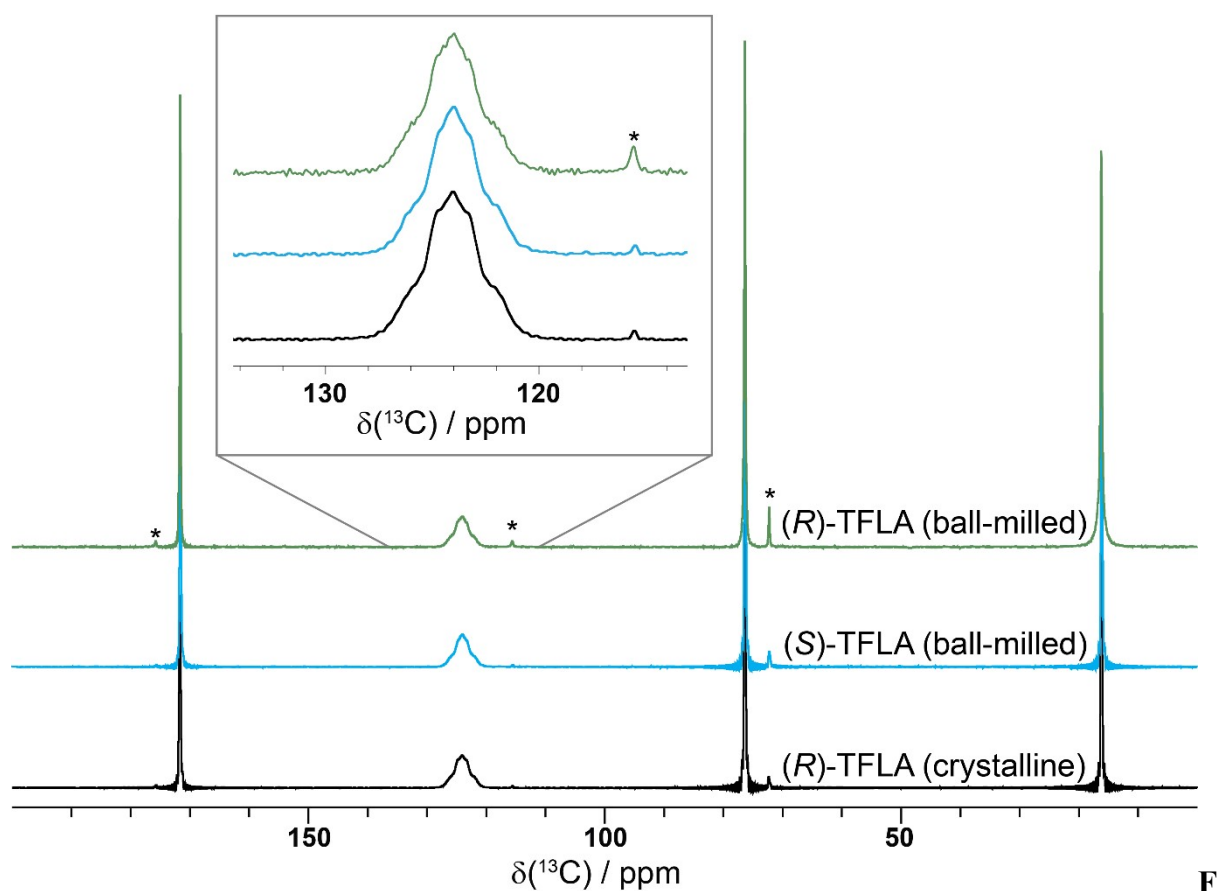
igure S1: ^{1}H-^{13}C CP spectra of crystalline and ball milled (*S*)- and ball milled (*R*)-TFLA recorded at 16.4 T using a MAS frequency of 17.5 kHz illustrate that the CF$_3$-line shape is conserved also for the (*R*)-TFLA enantiomer and that milling does not change the spectral features. The truncation visible in the spectra is related to insufficiently long acquisition times. * denote MAS spinning sidebands, which appear at the same position for all the three spectra.
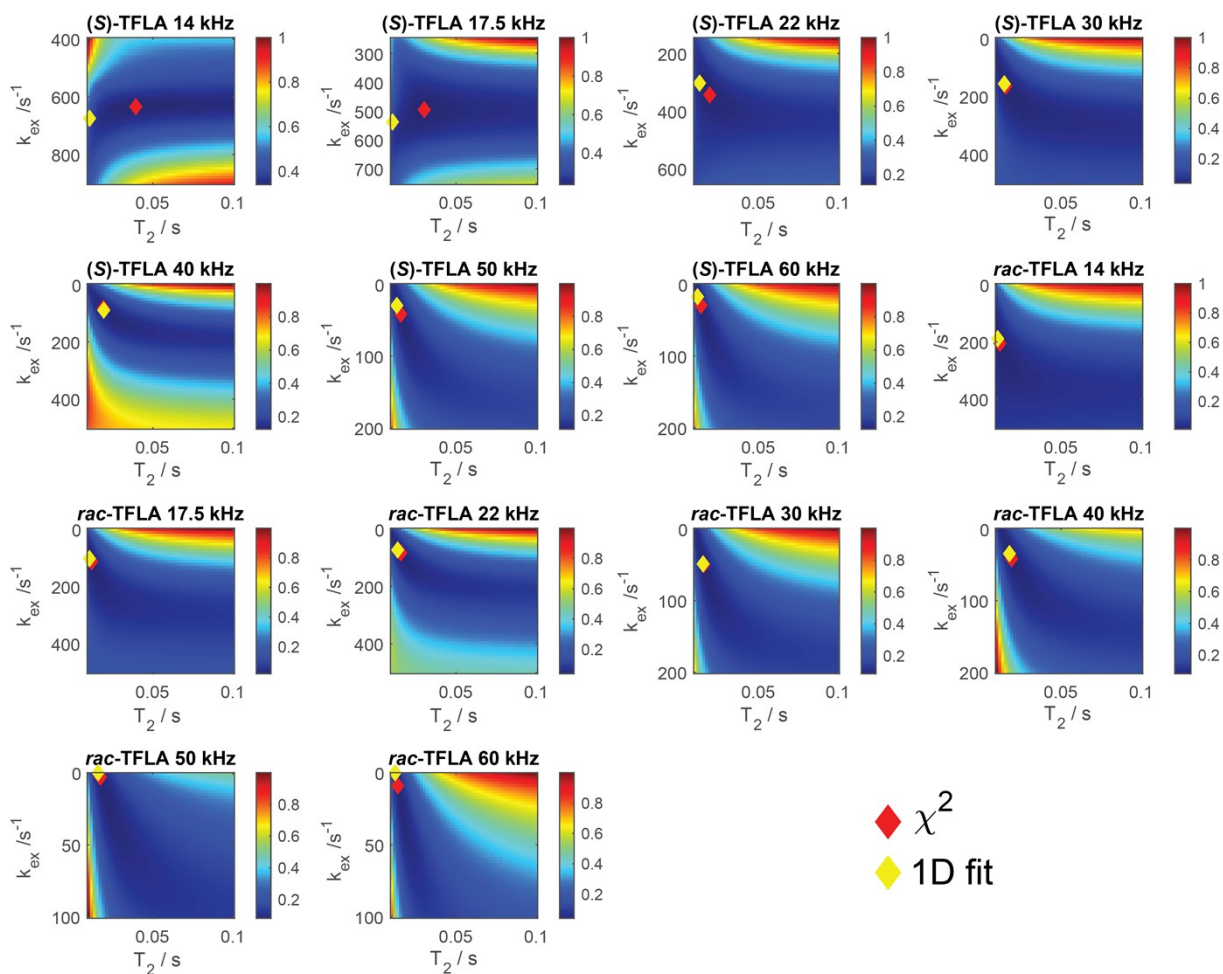
Figure S2: 2D contour plots for minimum χ^2-estimation with variable T_2- and k_{ex}-values reported for all the recorded experiments. The yellow and red marks in the 2D plots correspond to the minima obtained from the 1D least-square fits and those obtained from χ^2-estimation, respectively.
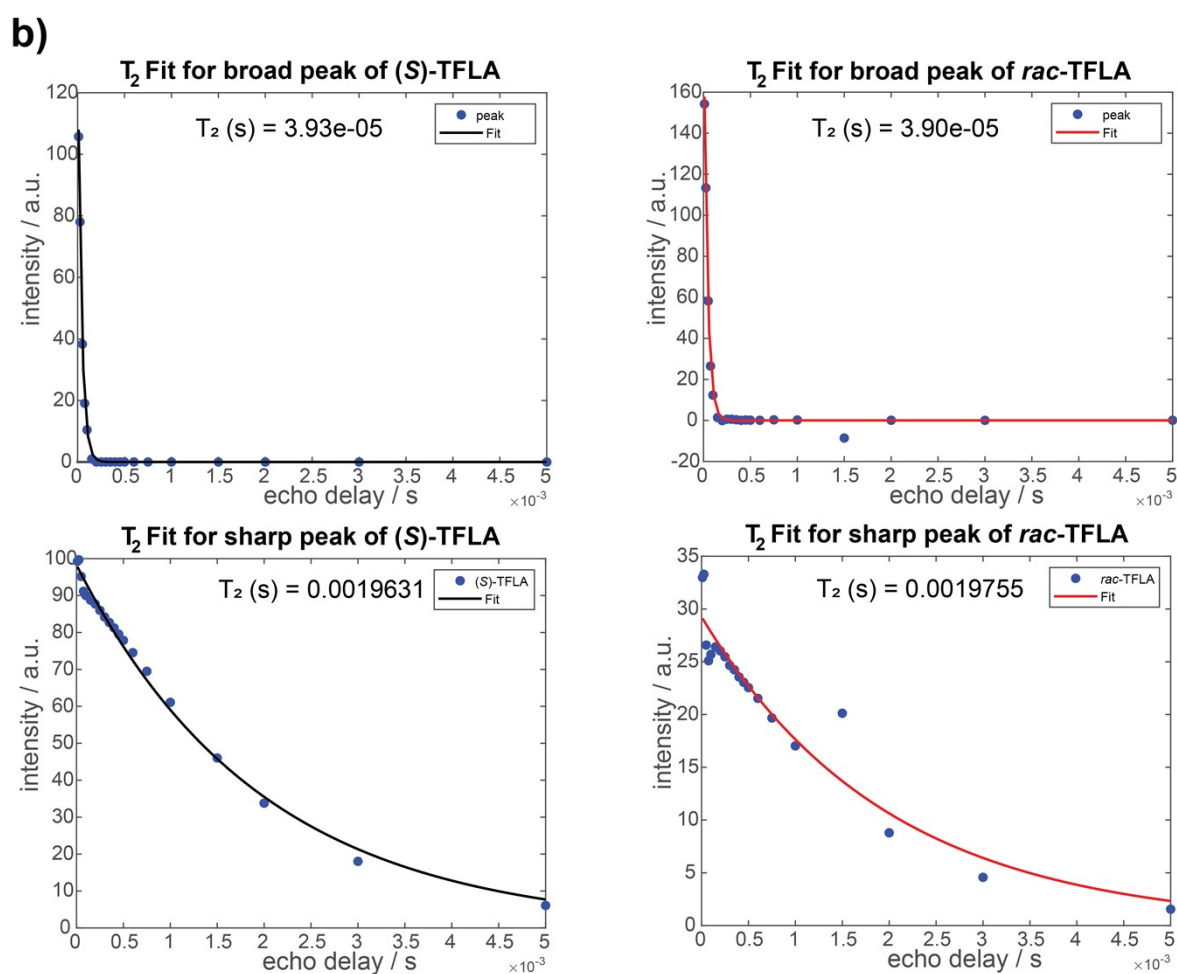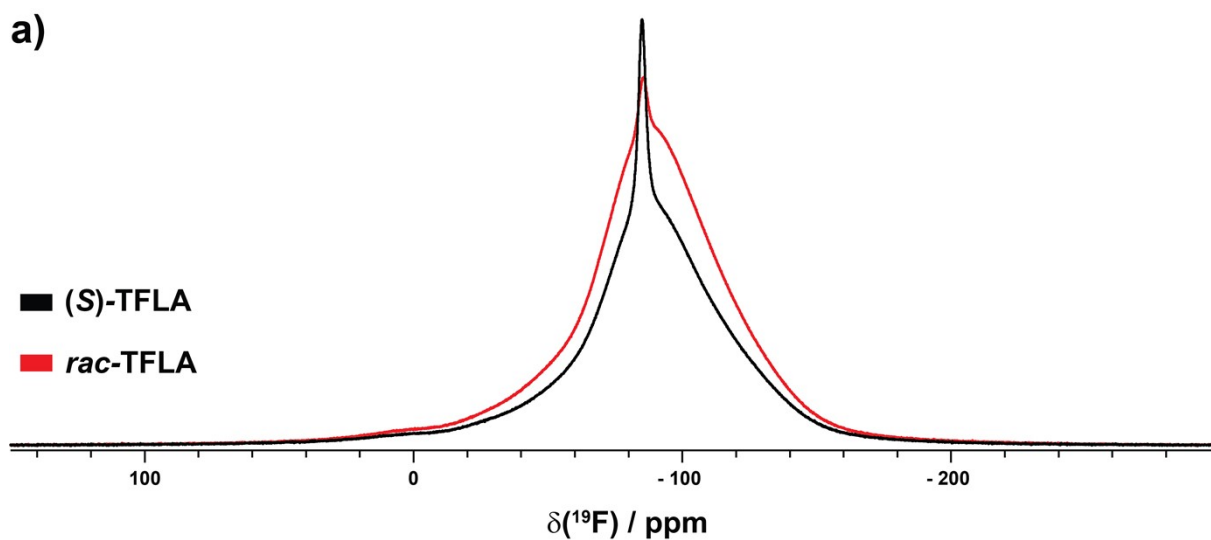
Figure S3: a) Static ^{19}F Hahn-echo spectra of *rac*- and (*S*)-TFLA recorded at 11.7 T static magnetic field strength. **b)** Static ^{19}F T_2 decay curves of *rac*- and (*S*)-TFLA recorded at 11.7 T static magnetic field strength. The solid lines correspond to the exponential decay fits.
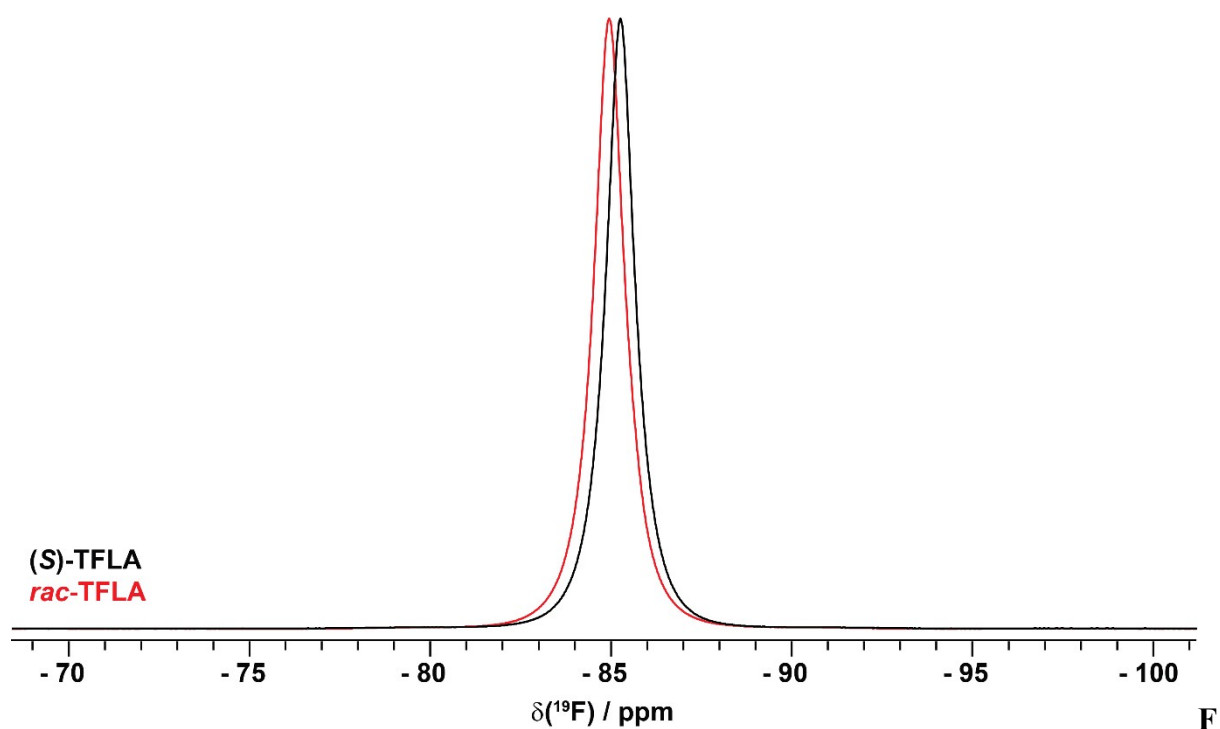
igure S4: ^{19}F Hahn-echo spectra of *rac*- and (*S*)-TFLA recorded at 17 kHz MAS and 11.7 T static magnetic field strength shows different CF_3 group ^{19}F chemical shifts for the racemic and enantiopure TFLA.
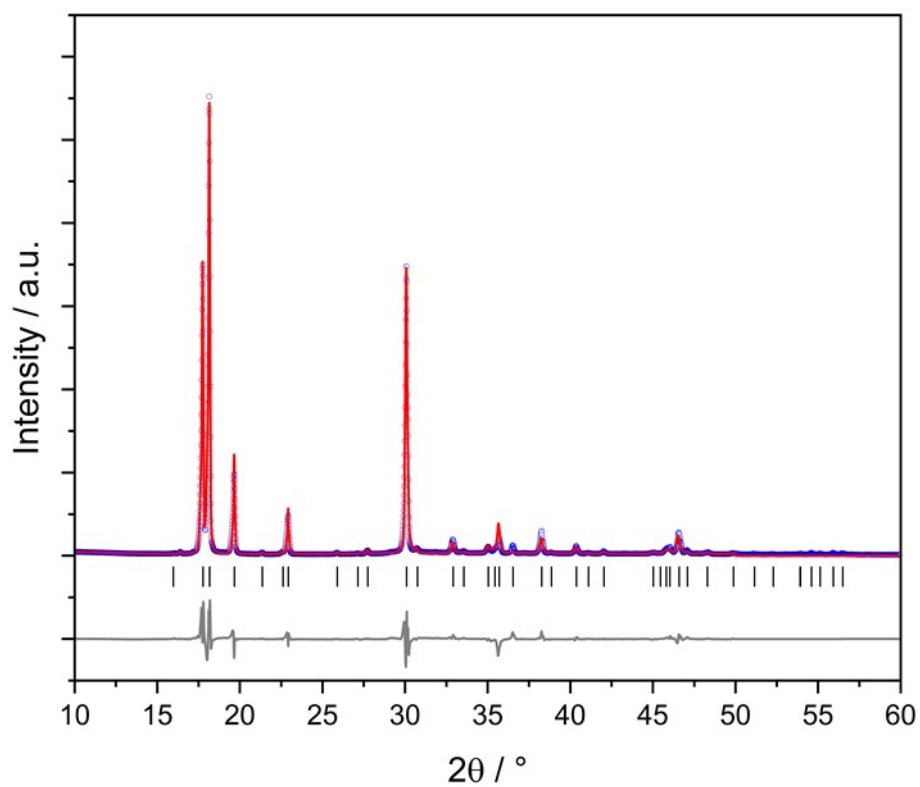
Figure S5: PXRD pattern of (*S*)-TFLA. The measured data are shown as circles, the fitted pattern is represented by the red line and the residual curve is shown in grey. The lines below the pattern represent the fitted peaks positions.
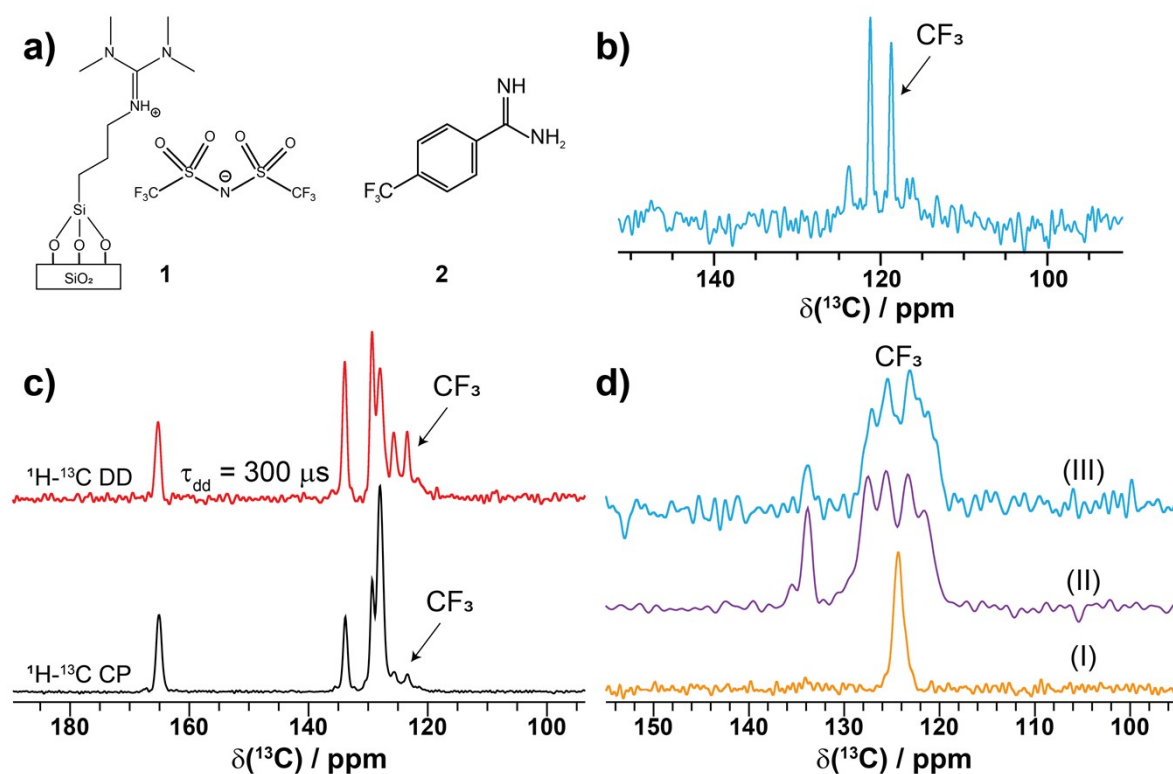
Figure S6: **a** Chemical structures of a SILP sample containing bistriflimide NTf_2^- **1** and 4-(trifluoromethyl)benzene-1-carboximidamide hydrochloride hydrate **2**. **b** ^{19}F-^{13}C CP spectrum recorded without ^{19}F decoupling of **1** shows a clearly resolved quartet. **c** ^1H-^{13}C CP and ^1H-^{13}C dipolar-dephasing ($\tau_{dd} = 300$ μs) ^{13}C-CP spectra of sample **2** bearing a CF_3 group. **d** ^{19}F-^{13}C CP spectra of sample **2** recorded with (I) ^{19}F high power decoupling, (II) ^1H 45 kHz decoupling and (III) without decoupling.

SI Tables

Table S: Overview about experimental parameters for solid-state NMR data in Figure 2

Sample	(S)-TFLA	rac-TFLA	(S)-TFLA	(S)-TFLA
Experiment	^{1}H-^{13}C CP MAS	^{1}H-^{13}C CP MAS	^{19}F-^{13}C CP MAS	^{19}F-^{13}C CP MAS
v_r / kHz	17.5	17.5	15	15
B_0 / T	16.4	16.4	11.7	11.7
Transfer I	H-C CP	H-C CP	F-C CP	F-C CP
$v_1(^1$H/^{19}F) / kHz	55	55	55	55
v_1(X) / kHz	45	45	45	45
Shape	Tangent shape			
^{13}C carrier / ppm	107	107	102	102
CP contact time / ms	4.5	4.5	3	3
t_1 increments	3072	3072	3072	3072
Sweep width (t_1) / ppm	567	567	795	795
Acquisition time (t_1) / ms	15.4	15.4	15.4	15.4
^{1}H/^{19}F Spinal64 decoupling / kHz	90	90	0	90
Interscan delay / s	8	8	8	8
Number of scans	1024	1024	128	128
T / K	255	255	270	270

Continued Table S2: Overview about experimental parameters for solid-state NMR data in Figure 4a

Sample	(S)-TFLA	(S)-TFLA	(S)-TFLA	(S)-TFLA	(S)-TFLA	(S)-TFLA	(S)-TFLA
Experiment	^{1}H-^{13}C CP MAS	^{1}H-^{13}C CP MAS	^{1}H-^{13}C CP MAS	^{1}H-^{13}C CP MAS	^{1}H-^{13}C CP MAS	^{1}H-^{13}C CP MAS	^{1}H-^{13}C CP MAS
v_r / kHz	14	17.5	22	30	40	50	60
B_0 / T	16.4	16.4	16.4	16.4	16.4	16.4	16.4
Transfer I	H-C CP						
$v_1(^1$H) / kHz	60	55	60	80	90	80	100
v_1(X) / kHz	40	45	46	58.3	61.6	40	53
Shape	Tangent shape						
^{13}C carrier / ppm	107	107	107	92	92	92	92
CP contact time / ms	4.5	4.5	4.5	4.5	4.5	4.5	4.5
t_1 increments	3072	3072	3072	3072	3072	3072	3072

Sweep width (t_1) / ppm	567	567	567	567	567	567	567
Acquisition time (t_1) / ms	15.4	15.4	15.4	15.4	15.4	15.4	15.4
^{1}H Spinal64 decoupling / kHz	90	90	90	90	90	90	90
Interscan delay / s	8	8	8	8	8	8	8
Number of scans	512	1024	512	6176	768	768	768
T / K	255	255	255	285	285	285	285

Continued Table S2: Overview about experimental parameters for solid-state NMR data in Figure 4b

Sample	*rac*-TFLA	*rac*-TFLA	*rac*-TFLA	*rac*-TFLA	*rac*-TFLA	*rac*-TFLA	*rac*-TFLA
Experiment	^{1}H-^{13}C CP MAS	^{1}H-^{13}C CP MAS	^{1}H-^{13}C CP MAS	^{1}H-^{13}C CP MAS	^{1}H-^{13}C CP MAS	^{1}H-^{13}C CP MAS	^{1}H-^{13}C CP MAS
v_r / kHz	14	17.5	22	30	40	50	60
B_0 / T	16.4	16.4	16.4	16.4	16.4	16.4	16.4
Transfer I	H-C CP						
v_1(^{1}H) / kHz	60	60	60	80	90	90	100
v_1(X) / kHz	46	42.5	38.2	58.3	60	40	53
Shape							
^{13}C carrier / ppm	129	129	129	119	119	119	119
CP contact time / ms	4.5	4.5	4.5	4.5	4.5	4.5	4.5
t_1 increments	3072	3072	3072	3072	3072	3072	3072
Sweep width (t_1) / ppm	567	567	567	567	567	567	567
Acquisition time (t_1) / ms	15.4	15.4	15.4	15.4	15.4	15.4	15.4
^{1}H Spinal64 decoupling / kHz	90	90	90	90	90	90	90
Interscan delay / s	8	8	8	8	8	8	8
Number of scans	256	256	256	768	768	5120	768
T / K	270	270	270	270	270	270	270

Continued Table S2: Overview about experimental parameters for solid-state NMR data in Figure 6a

Sample	*rac*-TFLA	*rac*-TFLA	*rac*-TFLA	*rac*-TFLA	*rac*-TFLA	*rac*-TFLA
Experiment	^{19}F-^{13}C CP MAS	^{19}F-^{13}C CP MAS	^{19}F-^{13}C CP MAS	^{19}F-^{13}C CP MAS	^{19}F-^{13}C CP MAS	^{19}F-^{13}C CP MAS
v_r / kHz	15	15	15	15	15	15
B_0 / T	11.7	11.7	11.7	11.7	11.7	11.7
Transfer I	F-C CP					
$v_1(^{19}F)$ / kHz	55	55	55	55	55	55
$v_1(X)$ / kHz	43.5	43.5	43.5	43.5	43.5	43.5
$v_{off}(^{19}F)$ / kHz	0	63.64	107.26	155.92	193.02	247.32
Θ /	90	54.7	40	30	25	20
Shape	Tangent shape					
^{13}C carrier / ppm	102	102	102	102	102	102
CP contact time / ms	3	3	3	3	3	3
t_1 increments	3072	3072	3072	3072	3072	3072
Sweep width (t_1) / ppm	795	795	795	795	795	795
Acquisition time (t_1) / ms	15.4	15.4	15.4	15.4	15.4	15.4
^{19}F CW decoupling / kHz	90	90	90	90	90	90
Interscan delay / s	8	8	8	8	8	8
Number of scans	1024	1024	1024	1024	1024	1024
T / K	270	270	270	270	270	270

Sample	(*S*)-TFLA	(*S*)-TFLA	(*S*)-TFLA	(*S*)-TFLA	(*S*)-TFLA	(*S*)-TFLA
Experiment	^{19}F-^{13}C CP MAS	^{19}F-^{13}C CP MAS	^{19}F-^{13}C CP MAS	^{19}F-^{13}C CP MAS	^{19}F-^{13}C CP MAS	^{19}F-^{13}C CP MAS
v_r / kHz	15	15	15	15	15	15
B_0 / T	11.7	11.7	11.7	11.7	11.7	11.7
Transfer I	F-C CP					
$v_1(^{19}F)$ / kHz	55	55	55	55	55	55
$v_1(X)$ / kHz	45.5	45.5	45.5	45.5	45.5	45.5
$v_{off}(^{19}F)$ / kHz	0	63.64	107.26	155.92	193.02	247.32
Θ /	90	54.7	40	30	25	20
Shape	Tangent shape					
^{13}C carrier / ppm	102	102	102	102	102	102
CP contact time / ms	3	3	3	3	3	3
t_1 increments	3072	3072	3072	3072	3072	3072
Sweep width (t_1) / ppm	795	795	795	795	795	795
Acquisition	15.4	15.4	15.4	15.4	15.4	15.4

time (t_1) / ms					
^{19}F CW decoupling / kHz	90	90	90	90	90	90
Interscan delay / s	8	8	8	8	8	8
Number of scans	1024	1024	1024	1024	1024	1024
T / K	270	270	270	270	270	270

Continued Table S2: Overview about experimental parameters for solid-state NMR data in Figure S1

Sample	(*S*)-TFLA	(*S*)-TFLA BM	(R)-TFLA BM
Experiment	^{1}H-^{13}C CP MAS	^{1}H-^{13}C CP MAS	^{1}H-^{13}C CP MAS
v_r / kHz	17.5	17.5	17.5
B_0 / T	16.4	16.4	16.4
Transfer I	H-C CP	H-C CP	H-C CP
v_1(^{1}H/^{19}F) / kHz	55	55	62
v_1(X) / kHz	45	45	44.5
Shape	Tangent shape		
^{13}C carrier / ppm	107	107	119
CP contact time / ms	4.5	4.5	1.5
t_1 increments	3072	3072	5120
Sweep width (t_1) / ppm	567	567	567
Acquisition time (t_1) / ms	15.34	15.4	25.6
^{1}H/^{19}F Spinal64 decoupling / kHz	90	90	90
Interscan delay / s	8	8	1.5
Number of scans	1024	512	5120
T / K	255	255	/

Continued Table S2: Overview about experimental parameters for solid-state NMR data in Figures S3 and S4

Sample	*rac*-TFLA	(*S*)-TFLA	*rac*-TFLA	(*S*)-TFLA
Experiment	^{19}F Hahn Eco	^{19}F Hahn Eco	^{19}F Hahn Eco	^{19}F Hahn Eco
v_r / kHz	0	0	17	17
B_0 / T	11.7	11.7	11.7	11.7
^{19}F carrier / ppm	−76	−76	−76	−76
t_1 increments	16384	16384	16384	16384
Sweep width (t_1) / ppm	1518	1518	212	212

Acquisition time (t_1) / ms	11.5	11.5	81.9	81.9
Interscan delay / s	3	3	3	3
Number of scans	32	32	32	32
T / K	/	/	275	275

Continued Table S1: Overview about experimental parameters for solid-state NMR data in Figure S6

Sample	Sample 1	Sample 2	Sample 2	Sample 2	Sample 2	Sample 2
Experiment	^{19}F-^{13}C CP MAS	^{1}H-^{13}C CP MAS	^{1}H-^{13}C DD 300µs MAS	^{19}F-^{13}C CP MAS	^{19}F-^{13}C CP MAS	^{19}F-^{13}C CP MAS
v_r / kHz	17	17	20	22	22	12.5
B_0 / T	11.7	11.7	11.7	11.7	11.7	11.7
Transfer I	F-C CP					
$v_1(^{19}$F) / kHz	60	60	55	60	60	50
v_1(X) / kHz	44	47.5	37	43	43	37.5
Shape	Tangent shape					
^{13}C carrier / ppm	102	101	102	99	99	89
CP contact time / ms	3	1.5	1.5	0.25	0.15	0.35
t_1 increments	3072	3072	3072	3072	3072	3072
Sweep width (t_1) / ppm	795	795	795	795	795	1241
Acquisition time (t_1) / ms	15.4	15.4	15.4	15.4	15.4	9.8
^{1}H /^{19}F decoupling / kHz	0	90	90	80	0	45
Interscan delay / s	7	15	10	15	15	7
Number of scans	4096	4096	2048	512	1280	9216
T / K	270	270	270	273	273	/

Table S3: Results from the Rietveld refinement of the (*S*)-TFLA PXRD

Parameters	Deposited Structure[20]	Refined Structure
a / Å	10.726(5)	11.055(4)
b / Å	5.892(2)	5.921(3)
c / Å	10.546(7)	10.809(4)
β / °	113.550(7)	113.565(3)
Cell Volume / Å^3	611.0(5)	648.6(5)

Supplementary references

1. C. Quaranta, I. d'Anciaes Almeida Silva, S. Moos, E. Bartalucci, L. Hendrickx, B. M. D. Fahl, C. Pasqualini, F. Puccetti, M. Zobel, C. Bolm and T. Wiegand, *Angew. Chem. Int. Ed. Engl.*, 2024, **63**, e202410801.
2. Y. Zhang, N. Levin, L. Kang, F. Muller, M. Zobel, S. DeBeer, W. Leitner and A. Bordet, *J Am Chem Soc*, 2024, **146**, 30057-30067.
3. B. M. Fung, A. K. Khitrin and K. Ermolaev, *J. Magn. Reson.*, 2000, **142**, 97-101.
4. R. S. Thakur, N. D. Kurur and P. K. Madhu, *Chem. Phys. Lett.*, 2006, **426**, 459-463.
5. D. Massiot, F. Fayon, M. Capron, I. King, S. Le Calvé, B. Alonso, J.-O. Durand, B. Bujoli, Z. Gan and G. Hoatson, *Magn. Reson. Chem.*, 2002, **40**, 70-76.
6. S. G. J. van Meerten, W. M. J. Franssen and A. P. M. Kentgens, *J. Magn. Reson.*, 2019, **301**, 56-66.
7. R. K. Harris, E. D. Becker, S. M. C. d. Menezes, P. Granger, R. E. Hoffman and K. W. Zilm, *Pure Appl. Chem.*, 2008, **80**, 59-84.
8. L. H. Rude, U. Filsø, V. D'Anna, A. Spyratou, B. Richter, S. Hino, O. Zavorotynska, M. Baricco, M. H. Sørby, B. C. Hauback, H. Hagemann, F. Besenbacher, J. Skibsted and T. R. Jensen, *Phys. Chem. Chem. Phys.*, 2013, **15**, 18185-18194.
9. OpenAI. (2023). ChatGPT (2024 version) [GPT-2023.2025 and GPT-2024o]. https://chat.openai.com/chat.
10. V. E. Zorin, S. P. Brown and P. Hodgkinson, *J. Chem. Phys.*, 2006, **125**, 144508.
11. S. Sturniolo, H. M. Wickins and P. Hodgkinson, *J. Chem. Phys.*, 2023, **158**, 244502.
12. S. A. Smith, T. O. Levante, B. H. Meier and R. R. Ernst, *J. Magn. Reson. A*, 1994, **106**, 75-105.
13. M. Ernst, H. Zimmermann and B. H. Meier, *Chem. Phys. Lett.*, 2000, **317**, 581-588.
14. M. P. Hanrahan, A. Venkatesh, S. L. Carnahan, J. L. Calahan, J. W. Lubach, E. J. Munson and A. J. Rossini, *Phys. Chem. Chem. Phys.*, 2017, **19**, 28153-28162.
15. A. Samoson, T. Tuherm and Z. Gan, *Solid State Nucl. Magn. Reson.*, 2001, **20**, 130-136.
16. G. Antonioli and P. Hodgkinson, *J. Magn. Reson.*, 2004, **168**, 124-131.
17. L. Müller and R. R. Ernst, *Mol. Phys.*, 1979, **38**, 963-992.
18. H. M. Rietveld, *Acta Cryst,*, 1967, **22**, 151-152.
19. R. W. Cheary and A. Coelho, *J. Appl. Crystallogr.*, 1992, **25**, 109-121.
20. V. A. Soloshonok, H. Ueki, M. Yasumoto, S. Mekala, J. S. Hirschi and D. A. Singleton, *J. Am. Chem. Soc.*, 2007, **129**, 12112-12113.
21. W. Dollase, *J. Appl. Crystallogr.*, 1986, **19**, 267-272.